CHEMISTRY OF MATERIALS
Cite This: Chem. Mater. 2018, 30, 4440−4447
Article
pubs.acs.org/cm

Synthesis of Mesoporous Germanium Phosphide Microspheres for High-Performance Lithium-Ion and Sodium-Ion Battery Anodes

Kuan-Wei Tseng, Sheng-Bor Huang, Wei-Chung Chang, and Hsing-Yu Tuan*

Department of Chemical Engineering, National Tsing Hua University, 101, Section 2, Kuang-Fu Road, Hsinchu, Taiwan 30013, ROC

Supporting Information

ABSTRACT: Germanium phosphide is a potential anode material because of its high theoretical capacity and incredible rate capability on lithium-ion batteries (LIBs) and sodium-ion batteries (SIBs). However, the huge volume change that occurs while germanium phosphide is converted to Na_3P or Li_3P directly leads to poor cyclability and limits further applications. Herein, mesoporous germanium phosphide ($MGeP_x$) microspheres with diameter size ranging from 0.5 to 1.5 μm were first prepared by a one-step and template-free approach. $MGeP_x$ microspheres were composed of nanoparticles of around 10 nm with a narrow distribution of pore sizes of around 4 nm. The $MGeP_x$ possessed superior features in LIBs/SIBs since it shortens the diffusion path of the energy carrier and provides the buffer space for the transport of Li/Na ions. $MGeP_x$ showed attractive electrochemical properties as a potential anode candidate, such as a high first-cycle Coulombic efficiency of 82.63%, high reversible capacity (1400 mA h g^{-1} after 150 cycles at 0.2 C), excellent ultrahigh rate capacity (370 mA h g^{-1} at 72 A g^{-1}, 40 C), and stable cycling performance (450 cycles at 1 C) in the LIBs and high reversible capacity (704 mA h g^{-1} after 100 cycles at 0.2 C) and stable cycling performance (200 cycles at 0.6 C) in SIBs.

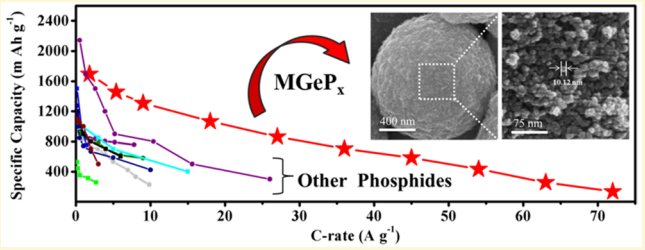

Phosphorus (P) is a promising candidate as an anode material for next-generation batteries because of the low cost due to its elemental abundance and its high theoretical capacity (2596 mA h g^{-1}) in lithium-ion batteries (LIBs) and sodium-ion batteries (SIBs) via the formation of Li_3P and Na_3P.[1,2] However, the volume changes of P converted to Na_3P and Li_3P are ∼500% and ∼300%, respectively, causing the pulverization of active materials and leading to the poor cycling performance.[1,3,4] To address this issue, it is suggested to synthesize a phosphide compound because of the synergistic effect between P and its pair element to alleviate strain during the ion insertion and desertion process.[5−8]

In general, phosphide anode materials react with Li through a conversion reaction as in the following formula:[9]

$$MP_x + 3xLi^+ \rightarrow M^0 + xLi_3P \qquad M = \text{metal}$$

Several phosphide materials such as Fe_2P,[7] NiP_2,[10] CuP_2,[11] and CoP[12] have been explored and shown improved cycle stability as anodes since these phosphides can mitigate the tension caused by volumetric changes through the metal matrixes.[13] However, specific capacities less than 1000 mA h g^{-1} were obtained since the metal matrixes are electrochemically inert materials with Li ions.[14]

The phosphide anode materials have active-matrix materials such as Zn−P-,[15] Sn−P-,[16] Si−P-,[17] and Ge−P-based systems in which elements are totally reactive toward the Li ion.[18] The concept of an active composite is to have different onset potentials such that one component is lithiated while the other one buffered the tension to alleviate the volume change.[19] The Si-based phosphides are attractive candidates due to their high theoretical capacity, but the challenge has been found that the cycle stability for the compound depends highly on the charge depth, and better reversibility could be achieved only charged to a limited state.[20] Compared to Si, Ge exhibits ∼400 times greater lithium-ion diffusivity and also 10^4 times intrinsic electronic conductivity higher than Si, which makes Ge able to operate at a high rate performance.[21] In addition, the unique electrochemical cycling properties (nearly isotropic lithiation) of Ge mitigating the high stresses were stated in the previous study, which was to be observed via *in situ* TEM study.[22] Unlike Si's inert characteristic with sodium, Ge can react with sodium by forming NaGe, making it a suitable element as a coupled element with P.

A lot of effort has been put into improving the reversibility and rate capability of the electrode by using nanostructured designs, especially porous structures which offer more efficient energy carrier (ion and electron) transport.[23−25] Methods to produce porous structures could be classified as template or template-free approaches.[26−29] In this work, we demonstrate the first example of template-free and one-step chemical synthesis for uniform mesoporous germanium phosphide ($MGeP_x$) microspheres composed of nanoparticles of around 10 nm with narrow distribution of pore sizes through a facile solvothermal approach. The growth route for $MGeP_x$ involved

Received: May 9, 2018
Revised: June 1, 2018
Published: June 2, 2018

DOI: 10.1021/acs.chemmater.8b01922
Chem. Mater. 2018, 30, 4440−4447

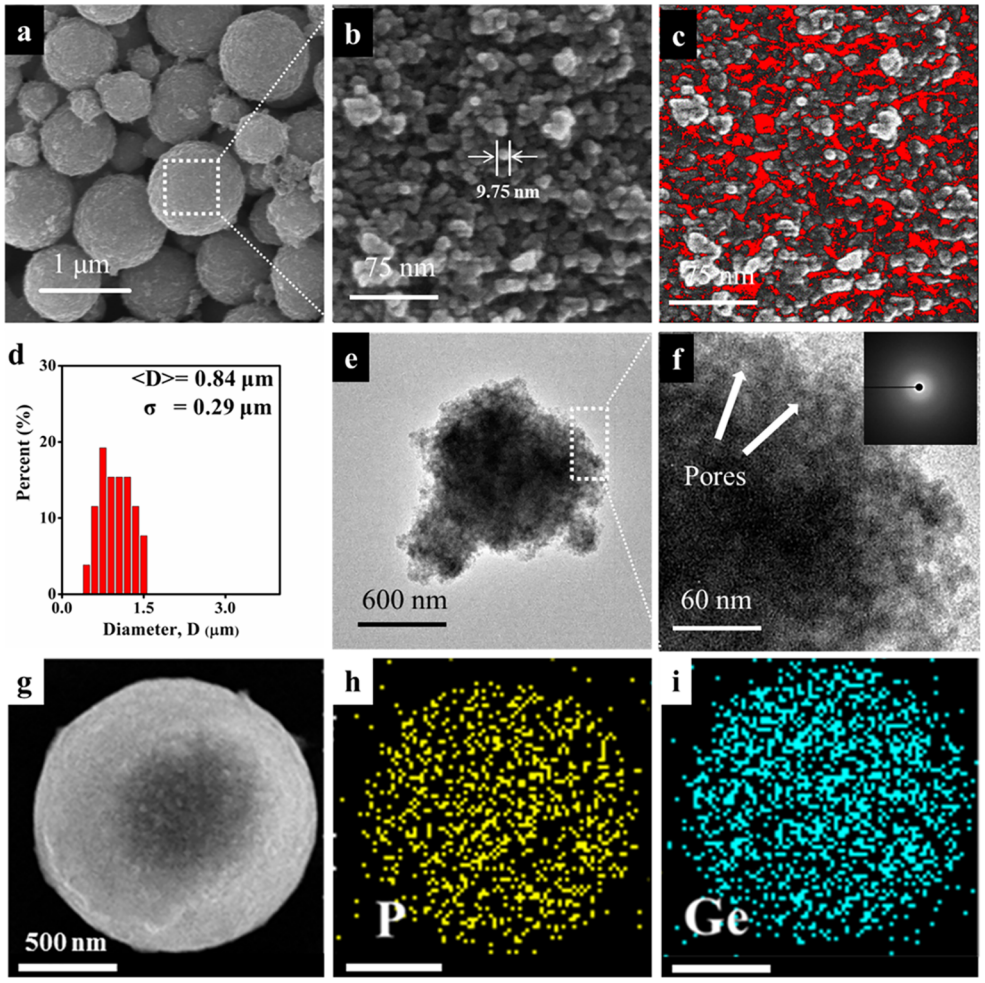

Figure 1. Mesoporous germanium phosphide ($MGeP_x$) microspheres were synthesized by TOP, DPG, and toluene at 430 °C. (a, b) SEM images for $MGeP_x$ from low magnitude to high magnitude. (c) Analysis of the void fraction in a $MGeP_x$ microsphere via the ImageJ software. The red color regions showed the void in the $MGeP_x$ microsphere. (d) Statistics of the $MGeP_x$ microsphere diameter. (e, f) TEM images for the $MGeP_x$ microsphere; the nanopores on the surface could be observed, and the SAED pattern of the $MGeP_x$ microsphere is in the inset of part f. (g–i) EDS mapping results of $MGeP_x$.

the formation of primary nucleation, diffusion of precursor monomer, and the good assembly of nanoparticles. More importantly, $MGeP_x$ exhibited outstanding electrochemical properties for both LIBs and SIBs. High specific capacities of 1812 and 818 mA h g^{-1} could be obtained at 0.2 C for LIBs and SIBs, respectively. Long cycle reversibility could be maintained at 1 C without obvious decay in 450 and 200 cycles for LIBs and SIBs. Moreover, $MGeP_x$ showed excellent ultrahigh rate capacity, i.e., 370 mA h g^{-1} at 40 C, for LIBs and great high rate capacity, i.e., 130 mA h g^{-1} at 10 C for SIBs. In brief, high capacity, stable cycling performance, and ultrahigh rate capability might be attributed to the high-quality mesoporous structure that not only effectively buffers the volume change but also shortens the ion diffusion path via the porous channels.

RESULTS AND DISCUSSION

***M*GeP$_x$ Characterization.** $MGeP_x$ microspheres were synthesized in the titanium reactor by using tri-*n*-octylphosphine (TOP), diphenylgermanium (DPG), and toluene at 430 °C for 10 min. Approximately 40 mg of black brown products with a high yield of 77% was collected for characterization. The sphere-shaped structure with rough surface was from the assembly of nanoparticles (~10 nm) which was observed from SEM (Figure 1a,b). Regarding the morphology of $MGeP_x$, the diameter of microspheres, 0.5–1.5 μm, was obtained by statistical analysis (Figure 1d) over $MGeP_x$ microspheres measured from the SEM image. The fraction of voids in $MGeP_x$ microspheres was roughly estimated via ImageJ software in Figure 1c. (The software was applied to measure the intensity of each pixel in an image and show the histogram of intensity. The pore ratio was determined by calculating the pixel number in a specified range of intensity.) $MGeP_x$ microspheres were also confirmed by TEM images (Figure 1e,f). There were obvious porous characteristics, which provided the structure with larger surface area and superior ion diffusion path. The SAED pattern of $MGeP_x$ microspheres (Figure 1f) indicates its amorphous structure, and the corresponding results could be found in the XRD patterns (Figure S7). The EDS mapping results (Figure 1g–i) shows Ge and P uniformly distributed on the sphere-shaped structure which suggested that the elemental dispersion was homogeneous. Using the Brunauer–Emmett–Teller (BET) measurements, the quantitative information on the surface area was obtained in Figure 2. These results showed that $MGeP_x$ microspheres had a large surface area of 258 m^2 g^{-1}, and the narrow distribution of pore sizes was located at around 4 nm

DOI: 10.1021/acs.chemmater.8b01922
Chem. Mater. 2018, 30, 4440–4447

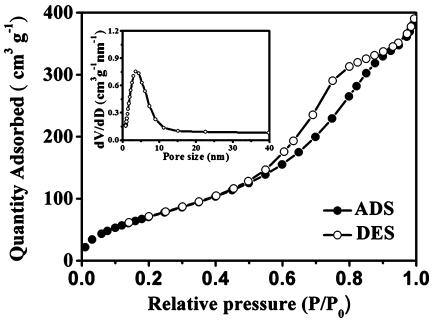

Figure 2. BET plot and corresponding pore size distributions (insets) of *M*GeP$_x$.

(Figure 2, inset). The composition of *M*GeP$_x$ was investigated by energy-dispersive spectrometry (EDS) data from STEM, and thermal gravimetric analysis (TGA) results were obtained. The TGA result showed that there was a sharp weight loss (37.2 wt %) between 450 and 500 °C, corresponding to the commercial red P as shown in Figure 3. The EDS result from STEM in Table 1 demonstrated that the weight ratio of P to Ge was 38.3 to 61.7. As a result, the value of x was around 1.5.

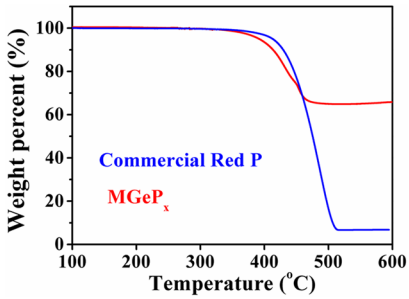

Figure 3. TGA measurement. The heating rate was set as 10 °C min^{-1}, and the flow rate was N_2 50 mL min^{-1}.

Table 1. STEM EDS Result of *M*GeP$_x$

element	wt %	atom %
P K	38.3	59.26
Ge K	61.7	40.74
total	100.0	100

The reaction process included high-temperature reduction of DPG into elemental germanium, followed by the catalytic cleavage of the strong P−C bond, and then the phosphorus was liberated from TOP, hence the primary germanium phosphide (GeP$_x$) nucleation.[30,31] It is a well-accepted theory for the metal phosphide to use TOP as its phosphorus source. The subsequent growth process involved diffusion of the precursor monomer and the surface reaction of the monomer. Under high temperature and high concentration, the nucleation and growth process would be accelerated and give the preferential spherical morphology products due to the minimization of the free energy of the whole system.[32,33] The occurrences of aggregation are the particle interactions including nucleation, growth, collision, and attachment which usually take place in the reaction solution without agitation.[34−37] Through the colloidal synthesis process, the variation in morphology of GeP$_x$ could be well-controlled by tuning the concentration of the reactant solution which was a key parameter in the synthesis system.[38,39] The formation mechanism was still not clear, but the possible growth path of the phenomenon was discussed (Figure 5). Solid GeP$_x$ (*S*GeP$_x$) was produced under concentrated TOP and DPG solution without adding any toluene (Figure 4a,b). The optimum reactant concentration was obtained by introducing 2 mL of toluene in the system (Figure 4e,f). The primary particle yielded small size (~10 nm), and narrow size distribution. The reason might be the coordination with the steric force and van der Waals force; the former one kept particles from directly coalescing, and the latter one shortened the distance of particles.[40] As a result, nanoscale pores formed during assembly of the primary particle which was reported in the previous work.[41] In Figure 4g,h, the concentration was diluted by adding 3 mL of toluene. The primary particles had large size and wide size distribution (10−50 nm). Imbalance of the steric force and van der Waals force made the aggregation uncontrollable and finally produced the huge cluster.[42] To further confirm these phenomena, the toluene was replaced with hexane and benzene and demonstrated the same trends (Figure S1).

The electrochemical properties of *M*GeP$_x$ as anode for LIB were tested in the coin cells, and a lithium metal foil was used as counter electrode operating in the voltage window 0.01−3 V versus Li/Li$^+$. Figure 6b shows that the first-cycle discharge and charge capacity of the *M*GeP$_x$ electrode with a loading ratio 55 wt % were 2126 and 1812 mA h g^{-1} at the current density 0.36

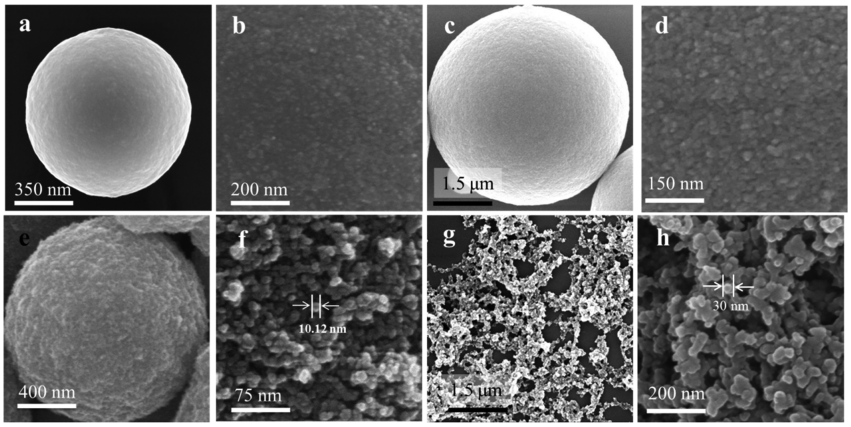

Figure 4. SEM image at low and high magnitude for GeP$_x$ synthesis using different amounts of toluene: (a, b) 0 mL, (c, d) 1 mL, (e, f) 2 mL, and (g, h) 3 mL, respectively.

DOI: 10.1021/acs.chemmater.8b01922
Chem. Mater. 2018, 30, 4440−4447

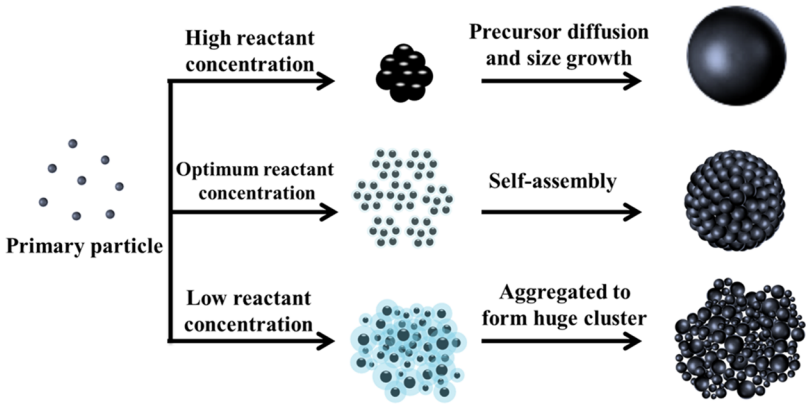

Figure 5. Schematic illustrations of possible growth routes of $SGeP_x$ and $MGeP_x$.

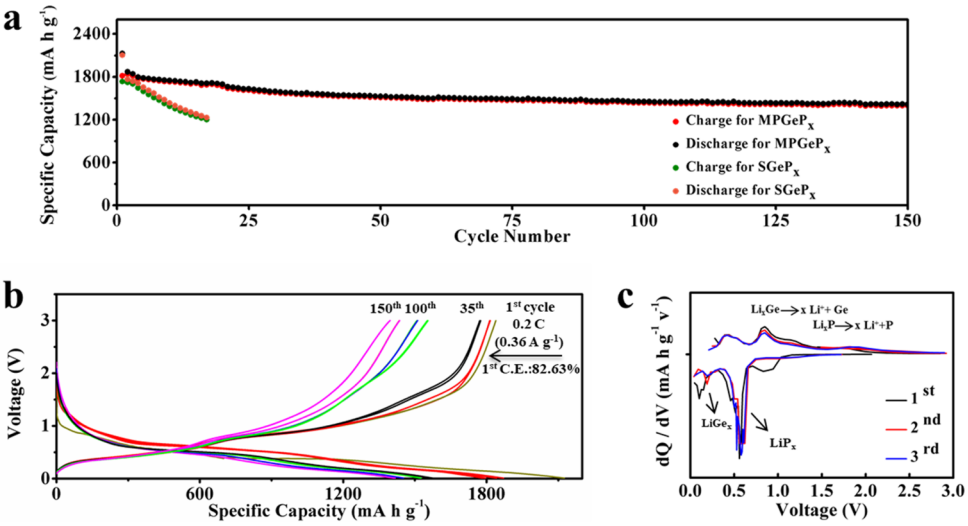

Figure 6. Electrochemical performance of GeP_x as anode for the LIB: 1 C rate = 1800 mA g^{-1}. (a) Cycling stability of the $MGeP_x$ and $SGeP_x$ at 0.2 C. (b) Lithiation/delithiation voltage profiles for $MGeP_x$ from the 1st to 150th cycles. (c) Differential capacity versus voltage for the first 3 cycles for $MGeP_x$.

A g^{-1} (0.2 C), demonstrating the high Coulombic efficiency of 82.63%. These results can be found in Figure 6a for both $MGeP_x$ and $SGeP_x$, indicating that it was not structure-dependent but corresponding to the material properties. A similar case has been reported for GeP_5/C composite, and the reason was the high conductivity of materials.[18] However, the cycle stability had an extreme difference between $MGeP_x$ and $SGeP_x$. The capacity decay of $SGeP_x$ was 31% (1733 to 1200 mA h g^{-1}) in 17 cycles (Figure S3a,b) because of the dramatic volume change during the lithiation/delithiation process. In contrast, $MGeP_x$ exhibited a high reversible capacity ~1400 mA h g^{-1} after 150 cycles with fine retention of 76.9% compared to the specific capacity of the first cycle (1812.9 mA h g^{-1}) which is resulted from the sufficient space of the porous structure that can buffer the volume change. The corresponding results could be observed by the cyclic voltammetry (CV) test. $SGeP_x$ (Figure S4a) exhibited the peak at 0.5 V in the negative scan which gradually shifted to lower voltage with the decaying of the current density, indicating the overpotential consuming the energy during the lithiation process. The peak at 1 V in the positive scan had disappeared after the first cycle which showed that the active materials lost activity because of the dramatic volume change during the lithiation/delithiation process. In contrast, the perfect overlap of the CV profiles in Figure S4b showed fine retention of $MGeP_x$. The peaks at 0.5 V (formation of lithium-rich alloy Li_xP) was followed by 0.1 V (formation of lithium-rich alloy Li_xGe) during the negative scan. The peaks at 0.5 V (delithiation of Li_xGe) and 1 V (delithiation of Li_xP) are in the positive scan. All results correspond to the previous work.[18]

Figure 6b presents the voltage versus capacity profiles. The differential capacity versus voltage plot was obtained in Figure 6c for the first three cycles of the $MGeP_x$ electrode. In the first-cycle lithiation (discharging process), the major peaks were quite distinct from the following cycle, which was due to the formation of the solid−electrolyte interphase (SEI) layer. Hence, starting with the second cycle, all the peaks were overlapped. The lithiation peaks at 0.1 and 0.56 V were attributed to the formation of different Li_xGe Li_xP alloys, and two obvious peaks at 0.4 and 0.85 V in the delithiation (charging process) corresponded to the extraction of lithium from lithium-rich alloys.[43,44]

The rate capability of $MGeP_x$ was studied at various rates by changing the different discharge−charge rates from 1 to 40 C (Figure 7a), and its voltage profiles were displayed in Figure 7b. Furthermore, the comparison among all GeP_x-related electrodes is also presented in Figure S8. $MGeP_x$ displayed outstanding performance at the rate tests, with current densities

DOI: 10.1021/acs.chemmater.8b01922
Chem. Mater. 2018, 30, 4440−4447

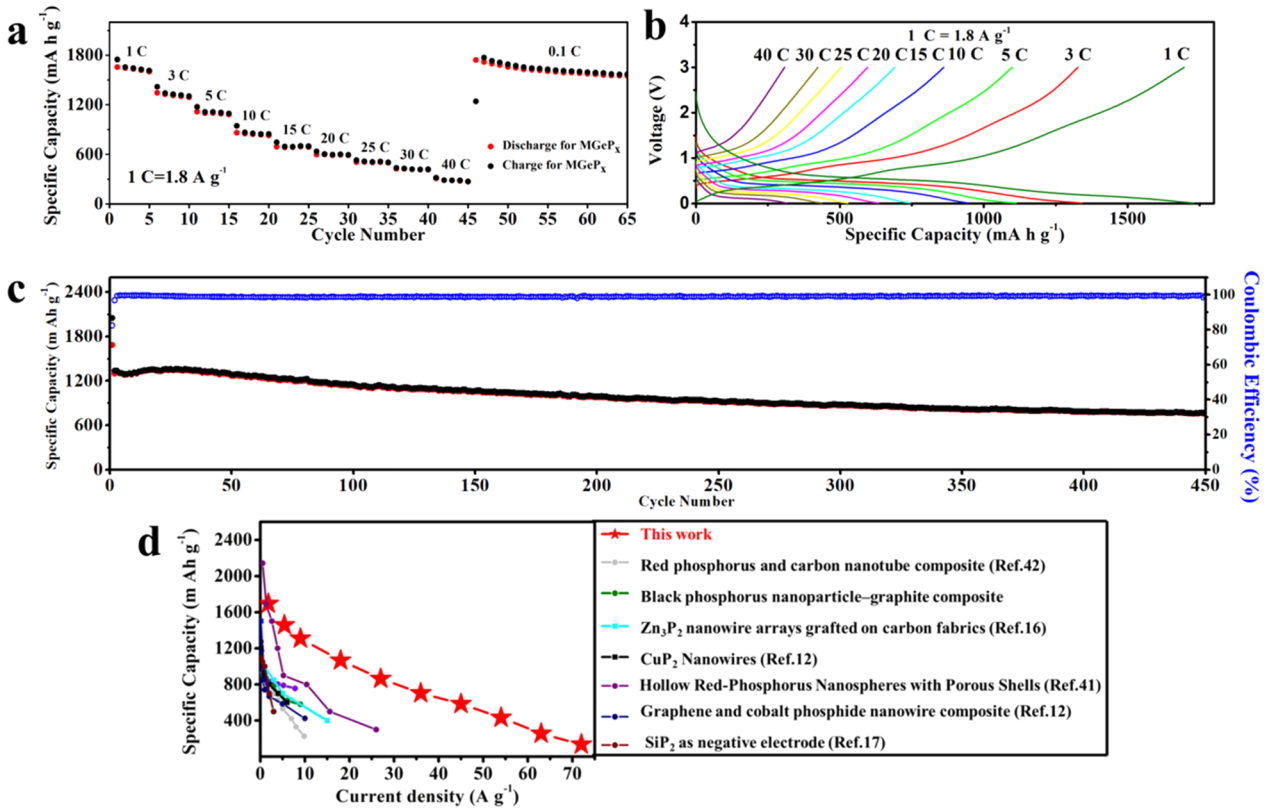

Figure 7. (a) The rate performance of the $MGeP_x$ electrode as anode for the LIB at the various current densities from 1 to 40 C and back to 0.1 C. (b) Corresponding potential profiles for $MGeP_x$ to part a. (c) Cycle performance for $MGeP_x$ at 1 C rate for 450 cycles. (d) Comparison of the specific capacities at various current densities for $MGeP_x$ with other anode materials related to phosphorus and phosphide in the literature.

of 1.8, 5.4, 9, 18, 27, 36, 45, 54, and 72 A g^{-1}, corresponding to the capacities of 1545, 1376, 1275, 1098, 922, 780, 661, 548, and 370 mA h g^{-1}. Furthermore, $MGeP_x$ exhibited no obvious capacity loss after 450 cycles at 1.8 A g^{-1} in Figure 7c. As seen in Figure 7d, the rate capacity has dominated over the other P-related anode materials in the LIBs.[4,11,12,16,20,45,46] In the meantime, electrochemical impedance spectroscopy (EIS) was carried to further study the interfacial electrochemical behavior of the $SGeP_x$- and $MGeP_x$-based electrode by the full charge/discharge cycling test at 1.8 A g^{-1} at frequencies ranging from 10 kHz to 10 mHz. Nyquist plots for electrodes at different cycles are presented in Figure S6. It comprised semicircles which were associated with a combination of charge-transfer and ohmic resistance at the high-frequency region. The straight line slope, at the low-frequency region, represented diffusion resistance. The proper electric equivalent circuit was fit in the inset of Figure S6. Comparing the results with $SGeP_x$ (Figure S6a) and $MGeP_x$ (Figure S6b), the fresh electrodes showed a slight difference between each other. Both electrodes demonstrated the smaller diameter of the semicircle after 50 cycles, indicating that the cycled electrodes possessed the smaller charge-transfer resistance than the fresh ones. However, the huge change for $SGeP_x$ in Figure S6a occurred after 75 cycles, which had a much higher impedance in comparison to the fresh cell. A similar result was reported in the previous work and led to a huge final capacity fade.[47] In Figure S6b, the charge-transfer resistance of the $MGeP_x$ electrode was nearly constant during cycling after 75 cycles, implicating that the charge-transfer pathway remained during the cycling process. Because of the formation of the SEI layer, the slope decreased continuously after 75 cycles, showing an increase of diffusion resistance, but electrodes still maintained high capacities demonstrating the fine ion diffusion path created by the porous structures.[48]

Germanium phosphide is also a potential anode material for SIBs because of the alloy formation of Na_3P and NaGe. As a result, $MGeP_x$ was tested by the half cell using sodium metal foil as a counter electrode for SIBs with the voltage window 0.01−2.0 V versus Na^+/Na. Figure 8a,b presents the cycle performance at 0.2 C (2400 mA g^{-1}) of the $MGeP_x$; the specific capacities of the first-cycle sodiation and desodiation were 1268 and 818 mA h g^{-1} indicating the first-cycle Coulombic efficiency of 65.28%. The huge capacity loss of 450 mA h g^{-1} in the first-cycle discharge/charge process corresponded to the electrolyte decomposition on the electrode surface for the formation of SEI. The high specific capacity 704 mA h g^{-1} could be maintained at 0.2 C over 100 cycles and 278 mA h g^{-1} at 1 C over 200 cycles in Figure 8c,f, demonstrating that the superior long cycle performance and the fluctuation of the capacity might be due to the temperature variations during the test, which had been mentioned in the previous literature.[49,50] The differential capacity versus voltage plot for $MGeP_x$ is presented in Figure S5b; the sodiation peaks in the 0.11 and 0.61 V could be observed in the first cycle which was attributed to formation of the SEI, and following cycles showed as well-overlapped below 0.6 V in the formation of sodium-rich NaGe, Na_3P alloys.[45,51] In the desodiation peak, there were two close peaks in the 0.54 and 0.86 V which represented the sodium-ion extraction from the sodium-rich product. A similar result could be confirmed in the cyclic voltammetry (CV) test (Figure S5a). Except for the first-cycle negative scan, a perfect overlap in the positive and negative scan showed the fine reversibility of

DOI: 10.1021/acs.chemmater.8b01922
Chem. Mater. 2018, 30, 4440−4447

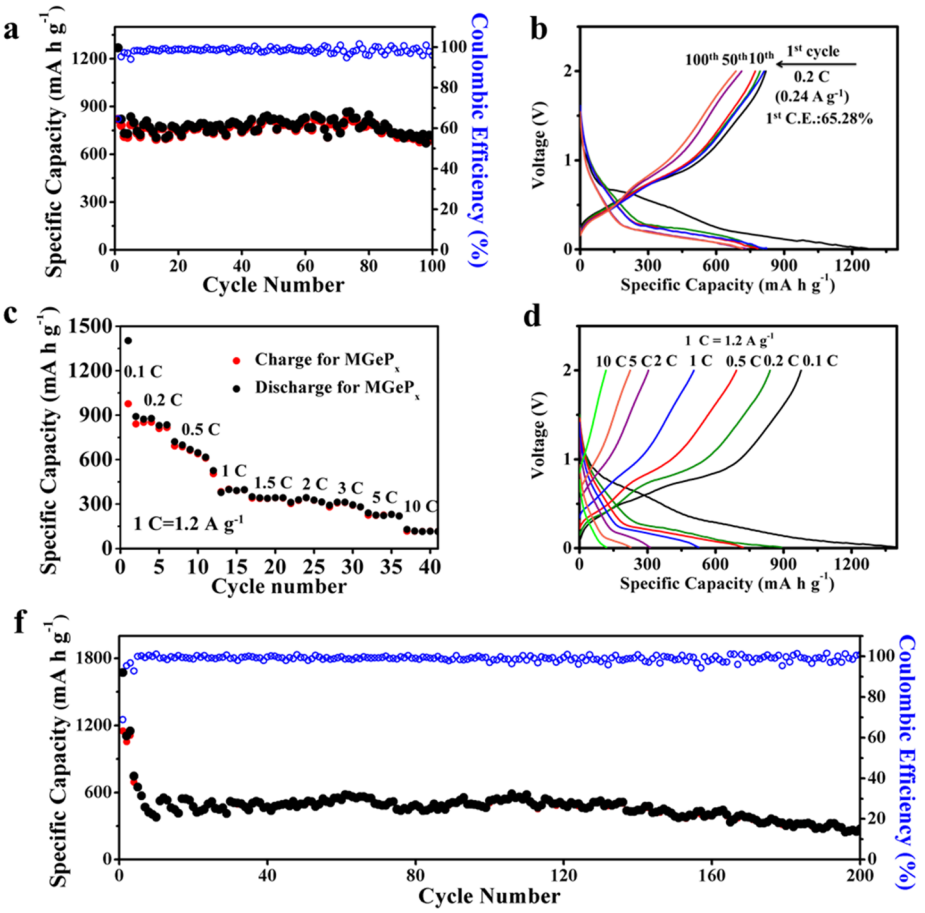

Figure 8. Electrochemical performance of $MGeP_x$ as anode for SIB: 1 C rate = 1200 mA g^{-1}. (a) Cycling stability of the $MGeP_x$ at 0.2 C. (b) Sodiation/desodiation voltage profiles for $MGeP_x$ from the 1st to 100th cycles. (c) Rate performance of $MGeP_x$ electrode as anode for the SIB at the various current densities from 0.1 to 10 C. (e) Corresponding potential profiles for $MGeP_x$ to part c. (f) Cycle performance for $MGeP_x$ at 1 C rate for 200 cycles.

$MGeP_x$. The rate capability of the $MGeP_x$ was also tested at the different discharge/charge rates from 0.1 to 10 C which is shown in Figure 8c, and its voltage profile is displayed in Figure 8d. $MGeP_x$ displayed a fine performance at the high rate test, with the capacity of 977, 840, 692, 400, 340, 320, 308, 230, and 117 mA h g^{-1} at different current densities of 0.12, 0.24, 0.6, 1.2, 1.8, 2.4, 3.6, 6, and 12 A g^{-1}, respectively.

As shown in the LIB and SIB test with the $MGeP_x$ anode, it is a promising anode material for both lithium and sodium storage. The outstanding electrochemical performance of $MGeP_x$ for Li ions and Na ions could be attributed to the mesoporous structure for advantages including (I) shorter diffusion path of the lithium ion and sodium ion in reaction with the GeP_x nanoparticles, (II) high-quality porous structure providing an environment for electrolyte penetration and increasing the efficiency of ion transport, and (III) the unique structure mitigating the volume expansion through the buffer space produced by the porous channel.

CONCLUSIONS

By the facile solvothermal method, we are able to synthesize the controllable porous structure without complex template fabrication processes. The common agents that are used as organic solvent (toluene, benzene, and hexane) played as the key factors making the nanoparticles assemble well and producing the high-quality mesoporous structure. Therefore, $MGeP_x$ demonstrates its high performances in both lithium and sodium storage including high energy density, ultrahigh rate capability, and superior cyclability. The superior electrochemical performance could be attributed to a shortened diffusion path for energy carriers in the solid phase and high specific area for facilitating reactivity. Similar reactions could introduce these kinds of stabilizing agents to fabricate the porous structure and enhance the performance in the energy storage, providing new opportunities to employ a more effective method for electrochemical devices.

EXPERIMENTAL SECTION

Materials. Diphenylgermane (DPG, 95%) was from Geleste. Tri-*n*-octylphosphine (TOP, 90%), anhydrous benzene (99.99%), anhydrous toluene (99.99%), anhydrous hexane (95%), ethanol (99.8%), poly(acrylic acid) (PAA, average Mv ≈ 300 000), and sodium hexafluorophosphate (98%) were from Sigma-Aldrich. Red phosphorus powder (98.9%) was purchased from Alfa Aesar. Celgard membrane, copper foil (0.01 mm), lithium foil (99.9%), electrolyte [1 M $LiPF_6$ in fluoro-ethylene carbonate/diethyl carbonate (FEC/DEC; 1:1 vol %)], Super P carbon black, and coin-typed cells (CR2032) were from SYNergy ScienTech Corp.

Synthesis of Different Morphologies of Germanium Phosphide (GeP_x). Upon tuning of the reactant concentration, the morphology of the GeP_x could be well-controlled. The same procedure was employed for each experiment. Typically, we prepared our reactant solution which contained 5 mL of TOP, 130 μL of DPG, and 2 mL of toluene in the 10 mL titanium reactor under the argon-

DOI: 10.1021/acs.chemmater.8b01922
Chem. Mater. 2018, 30, 4440−4447

filled glovebox. Then, the reactor was taken out, heated to 430 °C, and kept for 10 min. Finally, the reaction was stopped, and the whole system was cooled to the room temperature in the water bath. The products were cleaned with toluene several times until the supernatant solution was transparent. The residual solvent was removed by the vacuum-concentrated machine, and then, the final product $M\mathrm{GeP}_x$ was stored in the glovebox for the next application. To study the possible growth mechanism, we conducted a series of experiments with various amounts of toluene (0, 1, 2, and 3 mL) and species of agents (hexane and benzene).

Material Characterization. The structural studies of the different morphologies of germanium phosphide (GeP_x) were finished by SEM (HITACHI-SU8010) with energy-dispersive X-ray spectroscopy (HORIBA, EX- 250), TEM (TECNAI 20), and XRD (Rigaku Ultima IV). The composition investigations were carried out by TGA (SDT Q600) and STEM (JEOL, JEM-ARM200FTH).

Electrochemical Characterization. The well-dispersed elements containing active materials (55/50 wt %), conductive agent super P (30 wt %), and PAA binder (15%/20%) in deionized (DI) water and ethanol were in the formation of a high-quality slurry for the LIB/SIB anode electrode. Then, the prepared slurry was cast on a Cu foil uniformly and dried at 150 °C under argon gas for removing residual water followed by the rolling machine. Upon utilization with 0.1 μg resolution (Sartorius SE2), the weight of the electrode could be well-measured, and the loading of active materials was able to be calculated. The typical mass loading on the electrode was ~0.5 mg cm^{-2} (mass loadings of active material for LIBs/SIBs on the electrode were ~0.275/0.25 mg cm^{-2}). The coin-type half cell (CR2032), anode electrode, PP/PE/PP separator, glass fiber separator, and counter electrode lithium/sodium metal foil were assembled in the argon-filled glovebox. The electrolytes were 1 M LiPF_6 in fuoroethylene carbonate/diethylcarbonate (FEC/DEC) (1:1 vol %) for LIBs and 1 M NaPF_6 in fuoroethylene carbonate/diethylcarbonate (FEC/DEC) (15:85 vol %) for SIBs. The electrochemical performance of anode materials was carried out by employing Maccor Series 4000 instruments.[33]

■ ASSOCIATED CONTENT

Supporting Information

The Supporting Information is available free of charge on the ACS Publications website at DOI: 10.1021/acs.chemmater.8b01922.

Summary of experimental parameters related to the organic solvents, SEM images, and additional electrochemical characterization of *S*GePx and *M*GePx electrodes (PDF)

■ AUTHOR INFORMATION

Corresponding Author

*E-mail: hytuan@che.nthu.edu.tw. Phone: (886)3-571-5131, ext: 42509.

ORCID

Hsing-Yu Tuan: 0000-0003-2819-2270

Notes

The authors declare no competing financial interest.

■ ACKNOWLEDGMENTS

We acknowledge the financial support by the Ministry of Science and Technology through the grants of MOST 106-2221-E-007-081-MY3, 106-2628-E-007-005-MY3, and 103-2221-E-007-089-MY3.

■ REFERENCES

(1) Sun, J.; Lee, H.-W.; Pasta, M.; Yuan, H.; Zheng, G.; Sun, Y.; Li, Y.; Cui, Y. A phosphorene−graphene hybrid material as a high-capacity anode for sodium-ion batteries. *Nat. Nanotechnol.* **2015**, *10*, 980−985.

(2) Zhang, C.; Wang, X.; Liang, Q.; Liu, X.; Weng, Q.; Liu, J.; Yang, Y.; Dai, Z.; Ding, K.; Bando, Y.; Tang, J.; Golberg, D. Amorphous Phosphorus/Nitrogen-Doped Graphene Paper for Ultrastable Sodium-Ion Batteries. *Nano Lett.* **2016**, *16*, 2054−2060.

(3) Sun, J.; Lee, H.-W.; Pasta, M.; Sun, Y.; Liu, W.; Li, Y.; Lee, H. R.; Liu, N.; Cui, Y. Carbothermic reduction synthesis of red phosphorus-filled 3D carbon material as a high-capacity anode for sodium ion batteries. *Energy Storage Mater.* **2016**, *4*, 130−136.

(4) Sun, J.; Zheng, G.; Lee, H.-W.; Liu, N.; Wang, H.; Yao, H.; Yang, W.; Cui, Y. Formation of stable phosphorus−carbon bond for enhanced performance in black phosphorus nanoparticle−graphite composite battery anodes. *Nano Lett.* **2014**, *14*, 4573−4580.

(5) Liu, S.; Zhang, H.; Xu, L.; Ma, L.; Chen, X. Solvothermal preparation of tin phosphide as a long-life anode for advanced lithium and sodium ion batteries. *J. Power Sources* **2016**, *304*, 346−353.

(6) Lu, Y.; Zhou, P.; Lei, K.; Zhao, Q.; Tao, Z.; Chen, J. Selenium Phosphide ($\mathrm{Se}_4\mathrm{P}_4$) as a New and Promising Anode Material for Sodium-Ion Batteries. *Adv. Energy Mater.* **2017**, *7*, 1601973.

(7) Wang, Y.; Zhang, L.; Li, H.; Wang, Y.; Jiao, L.; Yuan, H.; Chen, L.; Tang, H.; Yang, X. Solid state synthesis of $\mathrm{Fe}_2\mathrm{P}$ nanoparticles as high-performance anode materials for nickel-based rechargeable batteries. *J. Power Sources* **2014**, *253*, 360−365.

(8) Zhang, W.-J. A review of the electrochemical performance of alloy anodes for lithium-ion batteries. *J. Power Sources* **2011**, *196*, 13−24.

(9) Cabana, J.; Monconduit, L.; Larcher, D.; Palacin, M. R. Beyond Intercalation-Based Li-Ion Batteries: The State of the Art and Challenges of Electrode Materials Reacting Through Conversion Reactions. *Adv. Mater.* **2010**, *22*, 170−192.

(10) Li, Q.; Ma, J.; Wang, H.; Yang, X.; Yuan, R.; Chai, Y. Interconnected $\mathrm{Ni}_2\mathrm{P}$ nanorods grown on nickel foam for binder free lithium ion batteries. *Electrochim. Acta* **2016**, *213*, 201−206.

(11) Li, G.-A.; Wang, C.-Y.; Chang, W.-C.; Tuan, H.-Y. Phosphorus-Rich Copper Phosphide Nanowires for Field-Effect Transistors and Lithium-Ion Batteries. *ACS Nano* **2016**, *10*, 8632−8644.

(12) Yang, J.; Zhang, Y.; Sun, C.; Liu, H.; Li, L.; Si, W.; Huang, W.; Yan, Q.; Dong, X. Graphene and cobalt phosphide nanowire composite as an anode material for high performance lithium-ion batteries. *Nano Res.* **2016**, *9*, 612−621.

(13) Lee, J.-M.; Jung, H.; Hwa, Y.; Kim, H.; Im, D.; Doo, S.-G.; Sohn, H.-J. Improvement of electrochemical behavior of $\mathrm{Sn}_2\mathrm{Fe}$/C nanocomposite anode with Al2O3 addition for lithium-ion batteries. *J. Power Sources* **2010**, *195*, 5044−5048.

(14) Jiang, J.; Li, Y.; Liu, J.; Huang, X. Building one-dimensional oxide nanostructure arrays on conductive metal substrates for lithium-ion battery anodes. *Nanoscale* **2011**, *3*, 45−58.

(15) Chen, J.-Y.; Chin, L.-C.; Li, G.-A.; Tuan, H.-Y. Zinc diphosphide nanowires: bismuth nanocrystal-seeded growth and their use as high-capacity lithium ion battery anodes. *CrystEngComm* **2017**, *19*, 975−981.

(16) Li, W.; Gan, L.; Guo, K.; Ke, L.; Wei, Y.; Li, H.; Shen, G.; Zhai, T. Self-supported $\mathrm{Zn}_3\mathrm{P}_2$ nanowire arrays grafted on carbon fabrics as an advanced integrated anode for flexible lithium ion batteries. *Nanoscale* **2016**, *8*, 8666−8672.

(17) Duveau, D.; Israel, S. S.; Fullenwarth, J.; Cunin, F.; Monconduit, L. Pioneer study of SiP_2 as negative electrode for Li- and Na-ion batteries. *J. Mater. Chem. A* **2016**, *4*, 3228−3232.

(18) Li, W.; Li, H.; Lu, Z.; Gan, L.; Ke, L.; Zhai, T.; Zhou, H. Layered phosphorus-like GeP_5: a promising anode candidate with high initial coulombic efficiency and large capacity for lithium ion batteries. *Energy Environ. Sci.* **2015**, *8*, 3629−3636.

(19) Yang, J.; Takeda, Y.; Imanishi, N.; Yamamoto, O. Ultrafine Sn and SnSb0. 14 Powders for Lithium Storage Matrices in Lithium-Ion Batteries. *J. Electrochem. Soc.* **1999**, *146*, 4009−4013.

(20) Kwon, H.-T.; Lee, C. K.; Jeon, K.-J.; Park, C.-M. Silicon Diphosphide: A Si-Based Three-Dimensional Crystalline Framework as a High-Performance Li-Ion Battery Anode. *ACS Nano* **2016**, *10*, 5701−5709.

DOI: 10.1021/acs.chemmater.8b01922
Chem. Mater. 2018, 30, 4440−4447

(21) Yuan, F.-W.; Tuan, H.-Y. Scalable Solution-Grown High-Germanium-Nanoparticle-Loading Graphene Nanocomposites as High-Performance Lithium-Ion Battery Electrodes: An Example of a Graphene-Based Platform toward Practical Full-Cell Applications. *Chem. Mater.* **2014**, *26*, 2172−2179.
(22) Liang, W.; Yang, H.; Fan, F.; Liu, Y.; Liu, X. H.; Huang, J. Y.; Zhu, T.; Zhang, S. Tough Germanium Nanoparticles under Electrochemical Cycling. *ACS Nano* **2013**, *7*, 3427−3433.
(23) Liu, B.; Soares, P.; Checkles, C.; Zhao, Y.; Yu, G. Three-Dimensional Hierarchical Ternary Nanostructures for High-Performance Li-Ion Battery Anodes. *Nano Lett.* **2013**, *13*, 3414−3419.
(24) Luo, B.; Zhi, L. Design and construction of three dimensional graphene-based composites for lithium ion battery applications. *Energy Environ. Sci.* **2015**, *8*, 456−477.
(25) Ngo, D. T.; Le, H. T. T.; Kim, C.; Lee, J.-Y.; Fisher, J. G.; Kim, I.-D.; Park, C.-J. Mass-scalable synthesis of 3D porous germanium-carbon composite particles as an ultra-high rate anode for lithium ion batteries. *Energy Environ. Sci.* **2015**, *8*, 3577−3588.
(26) Qie, L.; Chen, W.; Xu, H.; Xiong, X.; Jiang, Y.; Zou, F.; Hu, X.; Xin, Y.; Zhang, Z.; Huang, Y. Synthesis of functionalized 3D hierarchical porous carbon for high-performance supercapacitors. *Energy Environ. Sci.* **2013**, *6*, 2497−2504.
(27) Shim, J.; Lee, J.; Ye, Y.; Hwang, J.; Kim, S.-K.; Lim, T.-H.; Wiesner, U.; Lee, J. One-Pot Synthesis of Intermetallic Electrocatalysts in Ordered, Large-Pore Mesoporous Carbon/Silica toward Formic Acid Oxidation. *ACS Nano* **2012**, *6*, 6870−6881.
(28) Lin, T.; Chen, I.-W.; Liu, F.; Yang, C.; Bi, H.; Xu, F.; Huang, F. Nitrogen-doped mesoporous carbon of extraordinary capacitance for electrochemical energy storage. *Science* **2015**, *350*, 1508−1513.
(29) Li, D.; Kaner, R. B. Shape and Aggregation Control of Nanoparticles: Not Shaken, Not Stirred. *J. Am. Chem. Soc.* **2006**, *128*, 968−975.
(30) Henkes, A. E.; Vasquez, Y.; Schaak, R. E. Converting Metals into Phosphides: A General Strategy for the Synthesis of Metal Phosphide Nanocrystals. *J. Am. Chem. Soc.* **2007**, *129*, 1896−1897.
(31) Henkes, A. E.; Schaak, R. E. Trioctylphosphine: A General Phosphorus Source for the Low-Temperature Conversion of Metals into Metal Phosphides. *Chem. Mater.* **2007**, *19*, 4234−4242.
(32) Wan, Y.; Guo, Z.; Jiang, X.; Fang, K.; Lu, X.; Zhang, Y.; Gu, N. Quasi-spherical silver nanoparticles: Aqueous synthesis and size control by the seed-mediated Lee−Meisel method. *J. Colloid Interface Sci.* **2013**, *394*, 263−268.
(33) Bastús, N. G.; Comenge, J.; Puntes, V. Kinetically Controlled Seeded Growth Synthesis of Citrate-Stabilized Gold Nanoparticles of up to 200 nm: Size Focusing versus Ostwald Ripening. *Langmuir* **2011**, *27*, 11098−11105.
(34) Nguyen, T.-D.; Dinh, C.-T.; Do, T.-O. A general procedure to synthesize highly crystalline metal oxide and mixed oxide nanocrystals in aqueous medium and photocatalytic activity of metal/oxide nanohybrids. *Nanoscale* **2011**, *3*, 1861−1873.
(35) Hanus, L. H.; Sooklal, K.; Murphy, C. J.; Ploehn, H. J. Aggregation Kinetics of Dendrimer-Stabilized CdS Nanoclusters. *Langmuir* **2000**, *16*, 2621−2626.
(36) Joo, S. H.; Park, J. Y.; Tsung, C.-K.; Yamada, Y.; Yang, P.; Somorjai, G. A. Thermally stable Pt/mesoporous silica core-shell nanocatalysts for high-temperature reactions. *Nat. Mater.* **2009**, *8*, 126−131.
(37) Wang, G; Sæterli, R.; Rørvik, P. M.; van Helvoort, A. T. J.; Holmestad, R.; Grande, T.; Einarsrud, M.-A. Self-Assembled Growth of $PbTiO_3$ Nanoparticles into Microspheres and Bur-like Structures. *Chem. Mater.* **2007**, *19*, 2213−2221.
(38) Bock, C.; Paquet, C.; Couillard, M.; Botton, G. A.; MacDougall, B. R. Size-Selected Synthesis of PtRu Nano-Catalysts: Reaction and Size Control Mechanism. *J. Am. Chem. Soc.* **2004**, *126*, 8028−8037.
(39) Tao, A. R.; Habas, S.; Yang, P. Shape Control of Colloidal Metal Nanocrystals. *Small* **2008**, *4*, 310−325.
(40) Lu, Z.; Yin, Y. Colloidal nanoparticle clusters: functional materials by design. *Chem. Soc. Rev.* **2012**, *41*, 6874−6887.
(41) Xuan, S.; Wang, Y.-X. J.; Yu, J. C.; Cham-Fai Leung, K. Tuning the Grain Size and Particle Size of Superparamagnetic Fe3O4Microparticles. *Chem. Mater.* **2009**, *21*, 5079−5087.
(42) Bishop, K. J. M.; Wilmer, C. E.; Soh, S.; Grzybowski, B. A. Nanoscale Forces and Their Uses in Self-Assembly. *Small* **2009**, *5*, 1600−1630.
(43) Chang, W.-C.; Tseng, K.-W.; Tuan, H.-Y. Solution Synthesis of Iodine-Doped Red Phosphorus Nanoparticles for Lithium-Ion Battery Anodes. *Nano Lett.* **2017**, *17*, 1240−1247.
(44) Qian, J.; Qiao, D.; Ai, X.; Cao, Y.; Yang, H. Reversible 3-Li storage reactions of amorphous phosphorus as high capacity and cycling-stable anodes for Li-ion batteries. *Chem. Commun.* **2012**, *48*, 8931−8933.
(45) Kim, Y.; Park, Y.; Choi, A.; Choi, N.-S.; Kim, J.; Lee, J.; Ryu, J. H.; Oh, S. M.; Lee, K. T. An Amorphous Red Phosphorus/Carbon Composite as a Promising Anode Material for Sodium Ion Batteries. *Adv. Mater.* **2013**, *25*, 3045−3049.
(46) Zhou, J.; Liu, X.; Cai, W.; Zhu, Y.; Liang, J.; Zhang, K.; Lan, Y.; Jiang, Z.; Wang, G.; Qian, Y. Wet-Chemical Synthesis of Hollow Red-Phosphorus Nanospheres with Porous Shells as Anodes for High-Performance Lithium-Ion and Sodium-Ion Batteries. *Adv. Mater.* **2017**, *29*, 1700214.
(47) Jossen, A. Fundamentals of battery dynamics. *J. Power Sources* **2006**, *154*, 530−538.
(48) Cheng, Y.; Chen, Z.; Zhu, M.; Lu, Y. Polyacrylic Acid Assisted Assembly of Oxide Particles and Carbon Nanotubes for High-Performance Flexible Battery Anodes. *Adv. Ener. Mater.* **2015**, *5*, 1401207.
(49) Zhu, Y.; Wen, Y.; Fan, X.; Gao, T.; Han, F.; Luo, C.; Liou, S.-C.; Wang, C. Red Phosphorus−Single-Walled Carbon Nanotube Composite as a Superior Anode for Sodium Ion Batteries. *ACS Nano* **2015**, *9*, 3254−3264.
(50) Ren, W.; Zhang, H.; Guan, C.; Cheng, C. Ultrathin MoS_2 Nanosheets@Metal Organic Framework-Derived N-Doped Carbon Nanowall Arrays as Sodium Ion Battery Anode with Superior Cycling Life and Rate Capability. *Adv. Funct. Mater.* **2017**, *27*, 1702116.
(51) Li, W.-J.; Chou, S.-L.; Wang, J.-Z.; Liu, H.-K.; Dou, S.-X. Simply mixed commercial red phosphorus and carbon nanotube composite with exceptionally reversible sodium-ion storage. *Nano Lett.* **2013**, *13*, 5480−5484.

DOI: 10.1021/acs.chemmater.8b01922
Chem. Mater. 2018, 30, 4440−4447